TECHNICAL ARTICLE

Investigation of Solidification Behavior in a New High Alloy Ni-Based Superalloy

XINXU LI,[1,2] CHONGLIN JIA,[2,3] ZHOUHUA JIANG,[1] YONG ZHANG,[2] and SHAOMIN LV[2]

1.—School of Metallurgy, Northeastern University, Shenyang 110819, China. 2.—Science and Technology on Advanced High Temperature Structural Materials Laboratory, Beijing Institute of Aeronautical Materials, Beijing 100095, China. 3.—e-mail: biamjcl@163.com

While solidification behavior has been investigated in several nickel-based superalloys, few investigations have focused on the meticulous study of solidification behavior in such a highly alloyed and high γ' volume fraction-containing alloy as GH4151. In this study, several material characterization techniques were employed to identify phase types, illustrate the morphology of precipitates, and detect composition characteristics. In addition, differential scanning calorimeter and isothermal solidification quenching experiments were used to explain the solidification sequence. It has been confirmed that $(Nb,Ti)C$ carbides, η phase, eutectic $(\gamma + \gamma')$, Laves, Ni_5Ce, and γ' phase were found in the as-cast GH4151. The solidification sequence was determined as follows: $L \rightarrow L + \gamma \rightarrow L + MC \rightarrow L + \eta \rightarrow L + (\gamma + \gamma') \rightarrow L + Laves \rightarrow L+Ni_5Ce$, and $\gamma \rightarrow \gamma'$. Combined with electron probe micro-analysis, the results show that Nb, Ti, Mo, and V are significantly enriched in the interdendritic region, which has elemental degrees of segregation such that $Nb > Ti > Mo > V$, while Al, Co, Cr, W, and Ni are enriched within the dendritic arms, whose degree of segregation is $W > Al > Ni > Co > Cr$.

INTRODUCTION

The increased thrust-to-weight ratio in advanced aircraft demands higher inlet temperatures and increased turbine efficiency,[1] which require excellent thermal and mechanical properties of the superalloy used. GH4151 is a recently developed γ' precipitation-strengthened wrought nickel-based superalloy, characterized with a γ' phase precipitation volume fraction of around 52%, which can be employed to service temperatures of 750°C or above. In order to improve the high-temperature mechanical properties and long-term high-temperature stability, optimized compositions of GH4151 have been designed with 3.4% Nb content and a total content of Al, Ti, and Nb of up to c. 10%.[2] Due to complex chemistry compositions, GH4151's solidification path is complex and consists of binary, ternary, and quartenary precipitating reactions.[3–6] Moreover, topologically close-packed phases during

solidification seriously affect the mechanical properties and service behavior of alloys.[4,7–10] Therefore, the solidification behavior of GH4151 is of interest.

The determination of the solidification sequence is essential to understand the solidification behavior of any alloy. Thermal analysis techniques are often applied to investigate the solidification path and identify the reaction temperatures during the solidification process.[11–14] Miao et al. has used the differential scanning calorimetry (DSC) technique to understand the effects of P and B additions in the IN718 superalloy.[15] Differential thermal analyses (DTA) has been used to determine the solidification sequence in the Ni-based superalloy CMSX 10.[16] D'Souza et al. utilized a DTA-based method to determine the enthalpy change and solid fraction evolution of the IN738LC superalloy.[17] Besides the investigation of the solidification sequence, hot tearing is commonly encountered during solidification, and the formation of hot cracks is strongly affected by the liquid fraction in the final stages of solidification.[18–21] Therefore, the relationship between the residual liquid fraction and

temperature is an important one. The isothermal solidification and quenching (ISQ) experiment has been intensively carried out to evaluate the residual liquid volume fraction.[22,23] In addition, the residual liquid volume fraction of the K418 superalloy has been obtained using ISQ.[3]

Although solidification behavior has been investigated in several superalloys,[24–27] few investigations have focused on the meticulous study of solidification behavior in such a highly alloyed and high γ' volume fraction-containing alloy as GH4151. The aim of the present work is to systemically explore the solidification behavior of GH4151. The findings of this study can provide a theoretical foundation to control the metallurgical quality of GH4151 in ingot form.

MATERIALS AND METHODS

The temperatures of phase transformations during solidification were calculated by JmatPro. DSC and ISQ were employed to obtain solidification sequences and determine the relationships between liquid fraction and temperature. Identification of precipitates and as-cast microstructures were acquired by x-ray diffraction (XRD), optical microscopy (OM), scanning electron microscopy (SEM), energy dispersive spectroscopy (EDS), and electron probe microanalysis (EPMA).

Experimental Materials

The chemical composition of GH4151 was 3.7 Al, 2.8 Ti, 3.4 Nb, 11.9 Cr, 4.5 Mo, 15 Co, 2.7 W, 0.5 V, 0.06 C, trace Ce, and balance Ni (mass fraction). The sample employed in the present investigation was cut from a GH4151 ingot with a diameter of 80 mm produced by vacuum induction melting.

XRD Phase Identification

A sample $8 \times 20 \times 40$ mm was cut from the ingot and electrolyzed. The electrolyte was $C_3H_8O_3$(50 mL) + HCl(50 mL) + $C_6H_8O_7$ (10 g) + CH_3OH (900 mL), the current density was 0.1–0.2 A/cm^2, and the electrolytic temperature was 0–5°C. The anode sludge was washed 3 times with a citric acid aqueous solution and distilled water, cleaned with methanol, and then pumped and dried with a 0.2-μm organic filter membrane. The powder obtained was tested on D8 Discover XRD equipment, and the results were calibrated using Jade 6.5.

Thermodynamic Simulation of JmatPro

Studies have shown that some thermodynamic properties can be calculated by Java-based material properties (JmatPro) for most Ni-based superalloys.[28,29] Hence, JmatPro and a nickel-based superalloy database were used to calculate the solidification sequence and segregation behavior of GH4151. The three alloy compositions were input into the program to calculate the equilibrium phase diagram. The first composition was 3.6 Al, 2.7 Ti, 3.3 Nb, 11.8 Cr, 4.4 Mo, 14.9 Co, 2.6 W, 0.3 V, 0.05 C, and balance Ni. The second composition was 3.7 Al, 2.8 Ti, 3.4 Nb, 11.9 Cr, 4.5 Mo, 15 Co, 2.7 W, 0.5 V, 0.06 C, and balance Ni. The third composition was 3.8 Al, 2.9 Ti, 3.5 Nb, 11.9 Cr, 4.6 Mo, 15.1 Co, 2.8 W, 0.6 V, 0.07 C, and balance Ni. Mean values and standard deviations were calculated to evaluate error level. The temperature range of the simulation was set from 1000°C to 1400°C. The simulations returned results at intervals of 10°C until the calculation was completed. The phase equilibrium state was calculated according to the lowest Gibb's energy principle.

DSC Measurement

The DSC was carried out on a NETZSCH STA 404C instrument to reveal the solidification sequence of GH4151. The sample, with dimensions of 5×1 mm was placed in an alumina crucible and tested in an argon atmosphere. The maximum value of heating was set to 1400°C, while heating and cooling rates were controlled at 10°C/min. Prior to the experiment, heating and cooling curves in the case of a crucible without the sample were recorded as a baseline. The heating and cooling curves of the sample and crucible minus the baseline can be regarded as the heating and cooling curves of the sample. The solidus temperature was then obtained on the heating curve and the liquidus temperature was obtained on the cooling curve. The other temperatures of the phase transition took the average value of the two curves. Three samples were prepared and mean values and standard deviations were calculated to evaluate error levels.

ISQ Process

Isothermal solidification samples with a size of 8×7.5 mm were cut from center portions of the ingot with a diameter of 80 mm. The samples were placed into an alumina crucible and sealed with a mixture of alumina powder and silica solution. The sealed samples were heated to 1400°C, held for 10 min to ensure uniform melt composition, then cooled to different temperatures at 10°C/min, and finally, the high-temperature microstructure was retained by water quenching. The test temperature was set between 1150°C and 1340°C at intervals of 10°C. Three samples were prepared, and the mean values and standard deviations of the liquid fraction at every temperature were calculated to evaluate error levels.

Microstructure Examination

The specimens for OM and SEM were prepared in solutions of Cr_2O_3(15 g) + H_3PO_4 (150 ml) + H_2SO_4 (10 ml) and etched electrolytically at 3–4 V in an aqueous solution of 10% phosphoric acid,

respectively. A Leica DM6000M optical microscope and a Quanta 200FEG scanning electron microscope were employed to inspect the microstructure, and energy dispersive spectroscopy (EDS) was employed to perform semi-quantitative microanalysis of the precipitates. The volume fraction of the liquid phase in the quenched samples was measured by quantitative image analysis using Adobe Photoshop. An electron probe microanalyzer (EPMA; JXA-8100) was employed to measure the quantitative chemistry compositions and types of precipitates.

RESULTS AND ANALYSES

Solidification Simulation and Identification of Phases

The solidification simulation was calculated by JmatPro, as shown in Fig. 1a. The results indicate the initial formation temperature of the γ phase was 1334.2°C and the termination temperature was 1262.1°C. The initial formation temperature of MC carbides was 1311.1°C. In addition, the γ' phase precipitated from the matrix at 1166.5°C after complete solidification. The solidification sequence is similar to that of other superalloys.[30] The prediction was be verified by DSC and ISQ (see below).

Electrolytic extraction was implemented to characterize the minor secondary phases of GH4151. Most of the γ and γ' phases were removed by electrolytic corrosion, and the minor secondary phases were retained as powders. Based on the results exhibited in Fig. 1b, the γ matrix, γ' phase, (Nb,Ti)C carbides, η phase, and Laves phase were found in the as-cast GH4151.

The Original Microstructure of the Ingot

As shown in Fig. 2a, the microstructure of the as-cast GH4151 presents an obvious dendritic structure, including dendrite arms and interdendritic regions. The microstructure in the interdendritic regions is complex, as seen in Fig. 2b. Figure 2c and d shows the morphologies of secondary phases

under SEM and EPMA, respectively. The secondary phases in the interdendritic region were identified based on their chemistry as determined by EPMA. The results show that the composition of the ($\gamma + \gamma'$) eutectic was 14.15 Co, 0.92 W, 4.56 Al, 0.43 V, 5.62 Ti, 0.09 C, and balance Ni (mass fraction). The composition of the MC carbide was 56.34 Nb, 19.20 Ti, 12.3 C, and balance Ni. The composition of the η phase was 15.40 Co, 2.70 Al, 10.72 Nb, 7.20 Ti, and balance Ni. The composition of the Laves phase was 19.76 Co, 17.08 Cr, 3.61 W, 19.43 Mo, 18.12 Nb, 0.97 Ti, and balance Ni. The EPMA image of Ni_5Ce is shown in Fig. 2d, and the composition of the precipitation particles determined by EPMA were 9.35 Co, 3.67 Cr, 0.87 Al, 2.28 Nb, 16.10 Ce, and balance Ni. In addition, the Ni_5Ce phase was always located around the Laves phase, indicating that it was precipitated after the formation of this phase. In summary, secondary phases of GH4151 were identified, consisting of carbide, η phase, eutectic ($\gamma + \gamma'$), Laves phase, and Ni_5Ce phase. The results of the microstructure observation are consistent with the results of XRD.

The Solidification Sequence

DSC was carried out on the sample cut from the center of the ingot. The heating and cooling curves of DSC are presented in Fig. 3. From the full scale curve in Fig. 3a, four endothermic peaks can be identified from the heating curve, and three exothermal peaks are identified from the cooling curve. On the heating curve, the peak of the liquidus and solidus temperatures can be obtained. In addition, two apparent endothermic peaks were formed due to the existence of a certain amount of MC carbide and η phase. With reference to previous results,[31] the ($\gamma + \gamma'$) eutectic phase precipitates before the Laves phase during solidification. However, due to their low amounts, sufficient energy could not be discerned by DSC. After the sample was fully remelted at 1400°C, it was soaked in the liquidus condition for 7 min before re-solidifying at
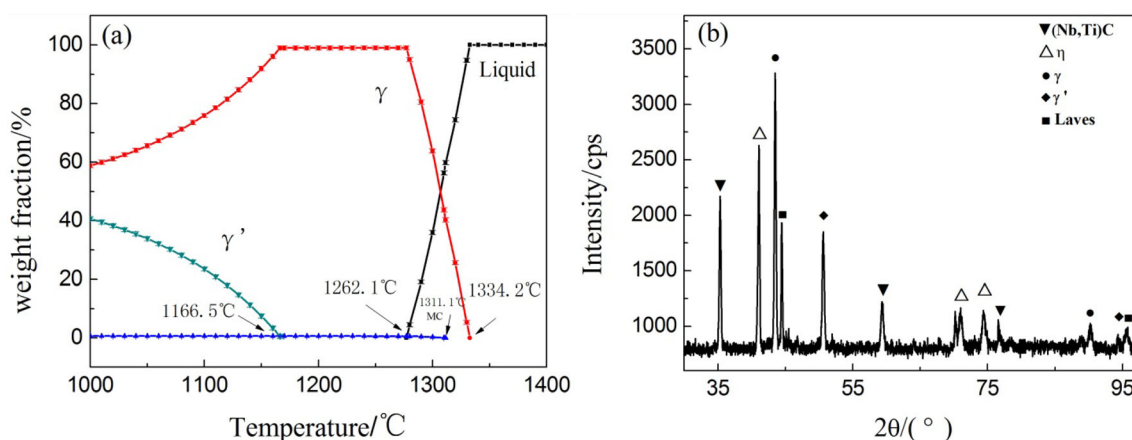

Fig. 1. (a) Calculated equilibrium phase diagram of GH4151 by JmatPro; (b) XRD patterns of as-cast GH4151.
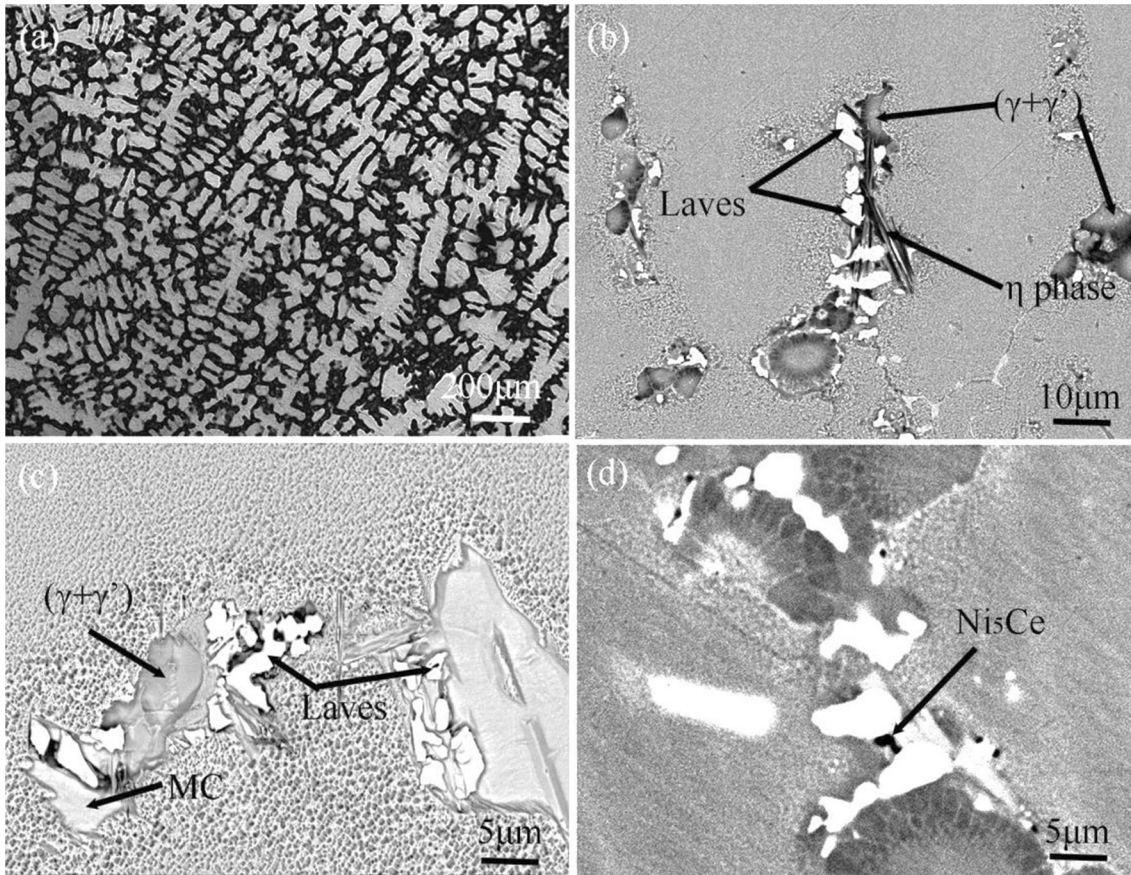
Fig. 2. The microstructure of the GH4151 ingot: (a) dendrite morphology under OM; (b) the morphology of the secondary phase under OM; (c) secondary phases under SEM; (d) morphology of secondary phase under EPMA.
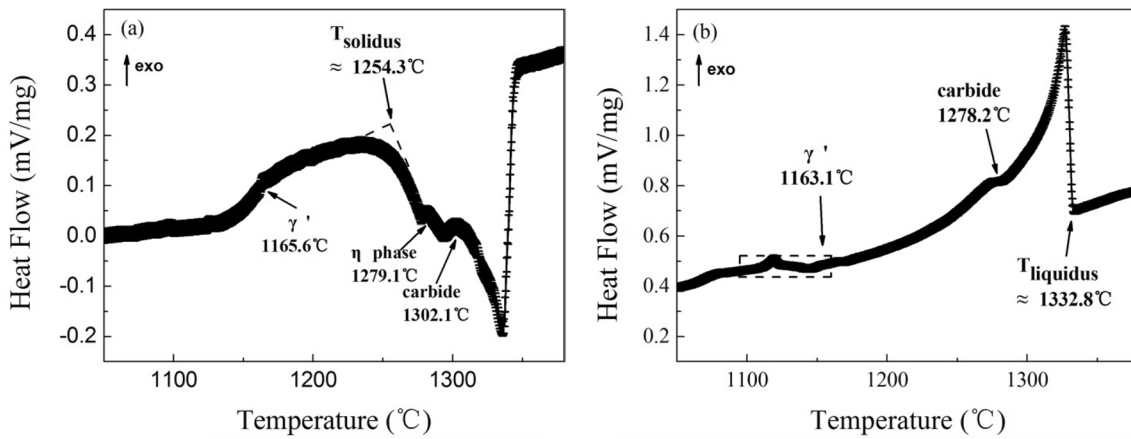

Fig. 3. DSC curves of GH4151: (a) on heating; (b) on cooling.

1332.8°C, which is deemed to make the solute distribution more homogeneous. In addition to the insufficient element segregation, the fast cooling rate during DSC is believed to further constrain the formation of large precipitates. As a result, no exothermal peaks of the η phase, eutectic $(\gamma + \gamma')$, and Laves phase were observed during the cooling process.

In brief, according to the heating curve, the transformation process of the phases in heating mainly includes: the γ' phase melting back into the matrix; the initial melting of the γ matrix; the dissolution of the η phase and carbides; and the complete melting of solid phase. According to the cooling curve, phase transformation in the cooling process mainly includes: the formation of γ

dendrites; the precipitation of carbides; and the precipitation of γ' out of the matrix. Due to the overheating effect during the heating process and the undercooling effect during the cooling process, the phase transition temperature of the heating process is higher than that of the cooling process.[32]

The Microstructure of ISQ Process

Figure 4 shows the microstructures of ISQ at different temperatures. The solidified and unsolidified regions can be clearly distinguished by the coarse and fine dendrites. Fully dendritic structures can be observed at both 1340°C and 1330°C, as shown in Fig. 4a and b, but the dendrite structure was much coarser at 1330°C, which revealed that a certain amount of the liquid phase had transformed into the solid phase. This indicates that the liquidus temperature is located between 1330°C and 1340°C. Inserting the intermediate value, the liquidus temperature is determined to be 1335°C. As the temperature further decreases, the solid fraction continues to increase.

It can be seen in Fig. 4c that the dendrites grew rapidly with the decreased temperature, and their volume fraction reached near 53.7% at 1320°C. At 1280°C (Fig. 4e), the liquid in the interdendritic region was still in a continuous state, and the volume fraction of the residual liquid was 35.1%. When the temperature dropped to 1260°C (Fig. 4f), the liquid channel between the dendrites was very narrow, but it was still connected by capillary action and the volume fraction of residual liquid reached 15.7%. At 1240°C (Fig. 4g), the distribution of the residual liquid phase presented the shape of isolated islands, indicating that there had been no solute diffusion between the isolated pools, with the residual liquid fraction remaining at 6%. The formation of micro-porosity in the as-cast superalloy is directly related to the transition from the continuous state of liquid channels to isolated pools, so 1260°C is an important temperature for GH4151. When the temperature reached 1220°C (Fig. 4h), there still existed 4.8% residual liquid. Up to 1150°C (Fig. 4i), the residual liquid disappeared. Therefore, the actual solidus temperature of the alloy should be 1150°C. The liquidus temperature obtained by DSC was 1252.2°C, while there still existed around 10% liquid phase in the ISQ sample. This phenomenon suggested that the solidus temperature obtained by DSC was a macroscopic result, which was 102.2°C higher than the microscopic solidus temperature
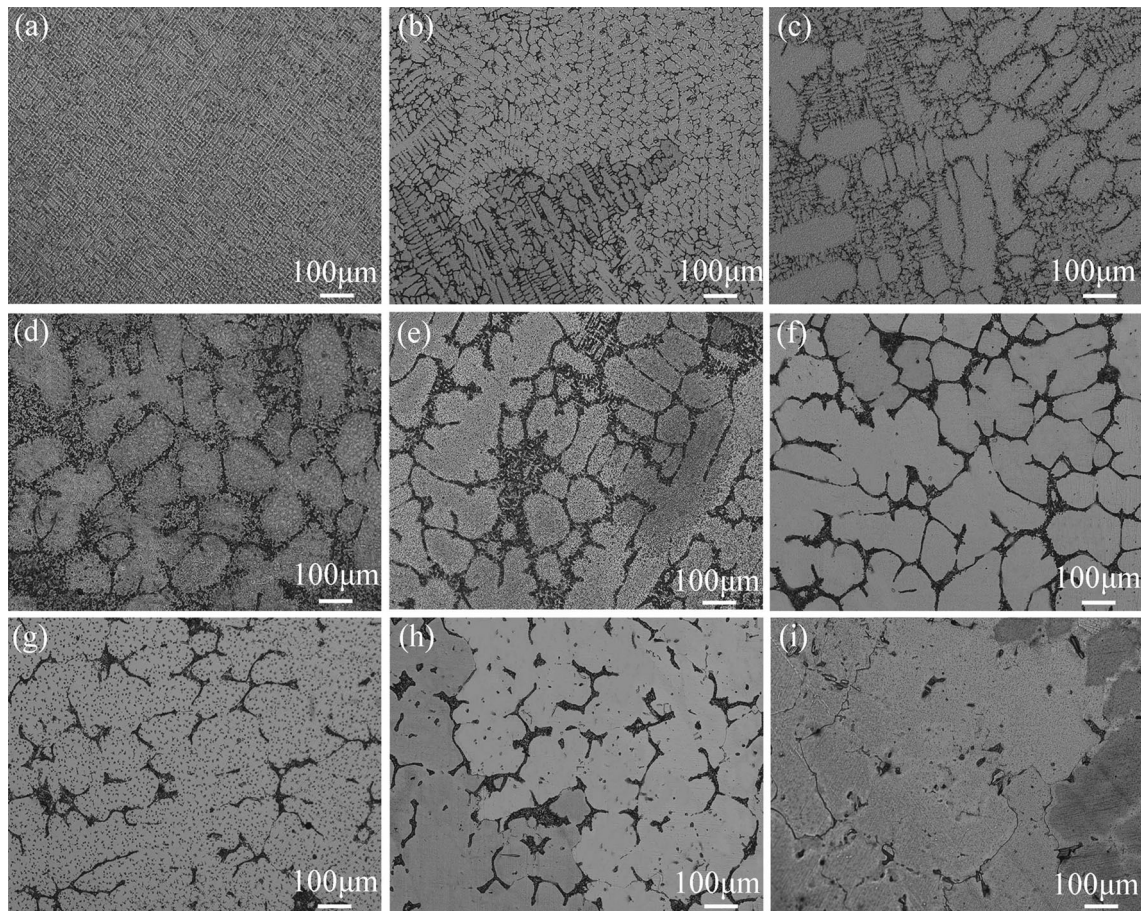

Fig. 4. Solidification microstructure of GH4151 quenched at different temperatures: (a) 1340°C; (b) 1330°C; (c) 1320°C; (d) 1300°C; (e) 1280°C; (f) 1260°C; (g) 1240°C; (h) 1220°C; (i). 1150°C.

obtained by ISQ. However, many low-melting phases, such as the eutetic ($\gamma + \gamma'$) and Laves phase, were formed in the temperature range of the macroscopic liquidus temperature and the microscopic liquidus temperature. When the temperature dropped to the microscopic solidus temperature, trace liquid existed in the form of a liquid film within the interdendritic region and the grain boundaries, which was closely related to casting cracking.

The precipitation temperatures of secondary phases are another concern in GH4151 during ISQ. The precipitation process of GH4151 during ISQ is shown in Fig. 5. At the isothermal temperature of 1300°C, MC carbides began to precipitate, which can be well distinguished in Fig. 5a. MC carbides would continue to precipitate in a subsequent solidification process. No new precipitates were detected until the temperature dropped to 1200°C (Fig. 5b). When the temperature dropped to 1200°C, the η phase was precipitated with the shape of thin strips. At the same time, the volume fraction of residual liquid remained at only 2.6%. At 1190°C, the formation of a "sunflower-shaped" eutectic ($\gamma + \gamma'$) phase was occasionally seen in the alloy, and the volume fraction of the residual liquid remained at 1.9% (Fig. 5c). At 1180°C, the formation of a white Laves phase occurred in the alloy, and the volume fraction of the residual liquid remained at 1.2% (Fig. 5d). A small amount of the residual liquid phase was still available at 1160°C, while secondary γ' began to precipitate from the matrix in the interdendritic regions. As shown in Fig. 5e, the secondary γ' presented a dendritic shape, indicating the slow cooling rate at that time. At 1150°C, more secondary

γ' phases were precipitated, and the residual liquid phase in the alloy basically disappeared, suggesting the end of the solidification process. Therefore, the solidus temperature of the alloy was 1150°C (Fig. 5-f). Trace amounts of Ni_5Ce formed next to the Laves phase in the later stage of solidification, but, due to too little content, the precipitation temperature could not be determined in ISQ.

A segregation coefficient, k, was defined for the elements as the ratio of the average concentration in the solid area to that in the liquid area, i.e., $k = C_s/C_l$.[33] Values of k less than 1 indicates that the elements segregate to the liquid regions and that these elements are regarded as positive segregation elements, while k values greater than 1 mean that the elements partition to the solid regions, and these elements are known as negative segregation elements.[34] It can be concluded from the EPMA quantitative analysis in Fig. 6 that positive segregation elements include Nb, Ti, Mo, and V, and that the order of segregation degree is Nb > Ti > Mo > V, while negative segregation elements include W, Al, Ni, Co, and Cr and the order of segregation degree is W > Al > Ni > Co > Cr.

DISCUSSION

The as-cast microstructure of GH4151 is complex. In order to improve the metallurgical quality of GH4151, it is essential to further analyze the solidification behavior. As verified by XRD, GH4151 consists of a γ matrix, γ' phase, (Nb,Ti)C carbides, η phase, Laves phase, and Ni_5Ce phase. The microstructures and results of EDS confirmed the existence of a ($\gamma + \gamma'$) eutectic phase. According
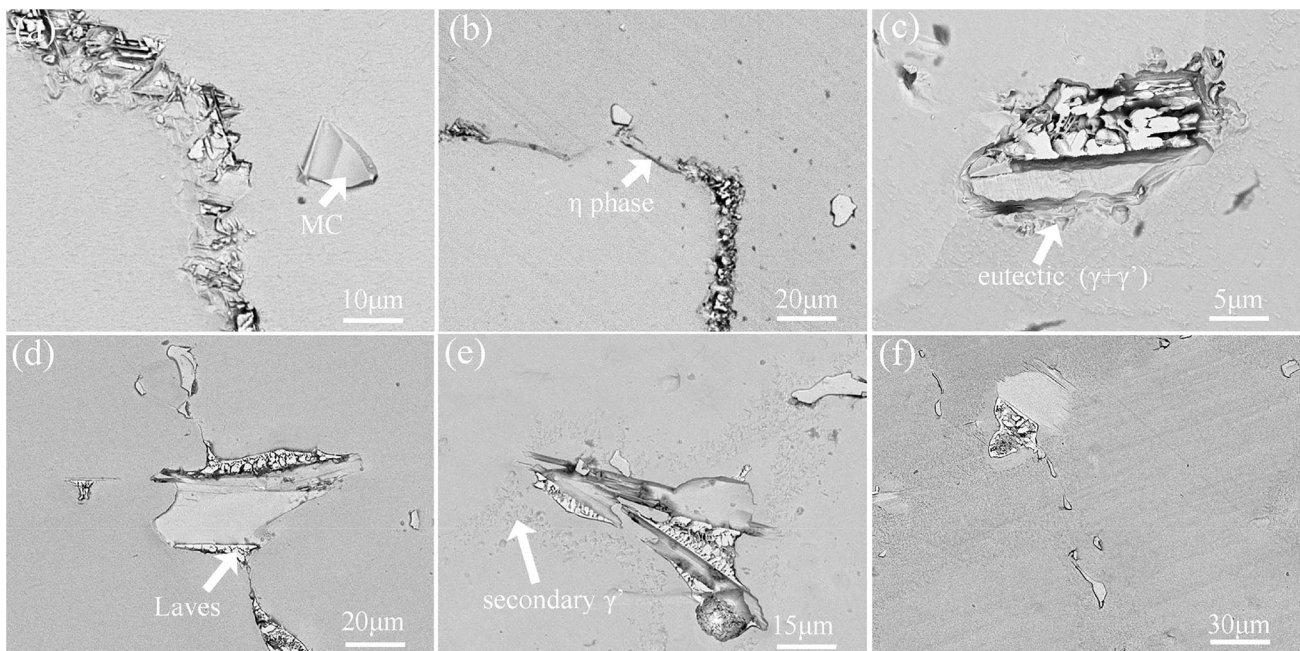

Fig. 5. Secondary phase during ISQ at different temperatures: (a) 1300°C; (b) 1200°C; (c) 1190°C; (d) 1180°C; (e) 1160°C; (f) 1150°C.

to the equilibrium simulations of JmatPro, GH4151 solidified under equilibrium conditions is free of the η phase, $(\gamma + \gamma')$ eutectic, Laves phase, and Ni_5Ce phase. With decreased temperature, the γ dendrite skeleton begins to form. The segregation of solute elements into the interdendritic regions resulted in nonequilibrium solidification. Therefore, the interdendritic regions became the position for the formation of the η phase, $(\gamma + \gamma')$ eutectic, Laves phase, and Ni_5Ce phase.

From the above experimental results, it has been shown that the area of carbides and eutectic $(\gamma + \gamma')$ in the interdendritic region is large. This is believed to be caused by high alloying elements, such as Al, Ti, and Nb. Nb performs a serious segregation inclination and forms a large amount of carbides, η phases, and Laves phases, which inevitably affect the number of reinforced phases and then reduce the properties of the alloy.

According to DSC and ISQ, the solidification sequence of GH4151 was obtained within the temperature range of the liquidus and solidus (Fig. 7a).
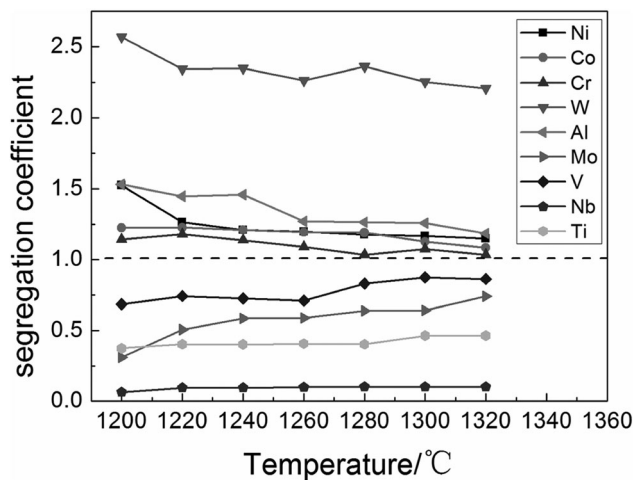

Fig. 6. Partition coefficients measured on the samples quenched at different temperatures.

Compared with the results of two experiment processes, the same solidification sequence can be obtained from JmatPro simulations. However, the temperature of phase transformation is different, especially the solidus temperature. This is attributed to inadequate diffusion of elements in the solid phase during the experiments. The volume fractions of the residual liquid of the quenching samples were determined by quantitative metallography, and the characteristic curve of isothermal solidification was finally made (Fig. 7b). T_L in Fig. 7 is the liquidus temperature and T is the ISQ temperature. It can be seen that the solidification rate of GH4151 is different at different solidification stages. The volume fractions of the residual liquid decreased sharply by about 65% within 35°C after the initial stage of solidification. However, in the range of 115–185°C below the liquidus temperature, only 7% was consumed, indicating that the liquid was solidified almost to a standstill.

In combination with XRD analyses, microstructure observations, DSC measurements, JmatPro simulations, and segregation of solute elements using EPMA, the solidification process of GH4151 takes place in the following stages. The solidification commences with the nucleation of the γ dendrites. Due to enrichment of the solute elements to the solid–liquid interface, the carbide precipitates first when it is sufficiently accumulated with positive segregation elements.[35] This is in accordance with the conclusions put forward in Ref. 33. With the precipitation of the carbides, Nb, Ti, and C will be depleted in the interdendritic region. In GH4151, the solute elements that exhibit the strong segregation tendency to liquid are the γ'-forming elements such as Nb and Ti.[36,37] Therefore, these elements will be continually accumulated in the interdendritic liquid and eventually generate the η phase and the eutectic $(\gamma + \gamma')$ phase.[38,39] As solidification goes on, Nb and Ti further enrich between the dendrites, which results in the formation of the Laves phase. Due to the low solubility of rare earth elements into the Laves phase, the segregation of Ce
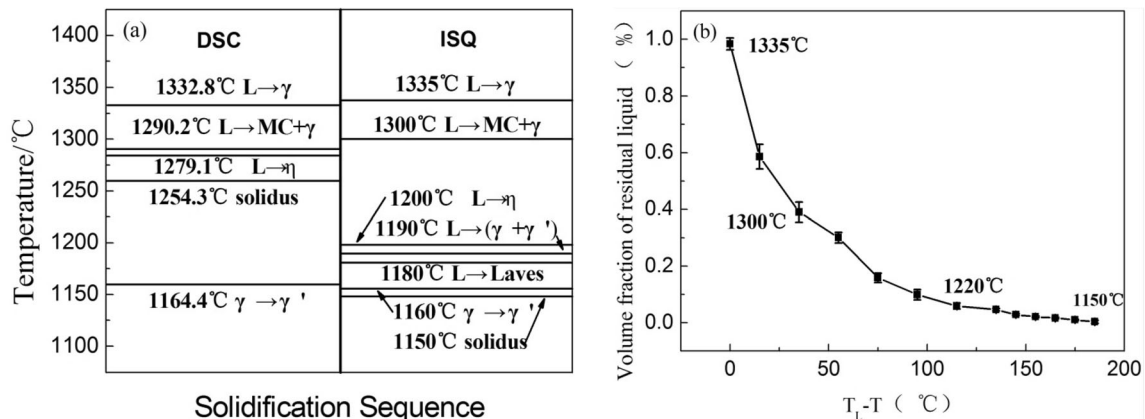

Fig. 7. (a) Solidification sequence; (b) characteristic curves of isothermal solidification for GH4151.

in the interdendritic regions becomes more serious in the last stage of solidification. Therefore, a Ni_5Ce phase forms around the Laves phase.

IMPROVING HOMOGENEITY OF THE ALLOY

Based on the solidification behavior and characteristics of GH4151, Nb was found to be very severely segregated in the interdendritic regions, and thus promoted the formation of brittle precipitates with other segregation elements, which leads to serious inhomogeneity for GH4151. In addition, the dissolution temperature of the carbides is relatively high and they are not redissolved in the homogenization process, so large-size carbides may become a source of cracking in subsequent hot working processes. Therefore, verification was carried out to improve the homogeneity of GH4151.

Three ingots were melted with a 30-kg induction furnace. The first ingot was melted normally, the content of C was reduced in the second ingot, and the contents of C and Nb elements were reduced in the third ingot. The chemical composition of Ingot 1 was 3.72 Al, 2.83 Ti, 3.51 Nb, 11.87 Cr, 4.54 Mo, 15.41 Co, 2.69 W, 0.6 V, 0.08 C, and balance Ni (mass fraction). The chemical composition of Ingot 2 was 3.71 Al, 2.84 Ti, 3.52 Nb, 11.90 Cr, 4.52 Mo, 15.37 Co, 2.71 W, 0.60 V, 0.04 C, and balance Ni. The chemical composition of Ingot 3 was 3.73 Al, 2.80 Ti, 3.20 Nb, 11.89 Cr, 4.51 Mo, 15.32 Co, 2.72 W, 0.60 V, 0.04 C, and balance Ni.

Figure 8a, b, and c illustrates the microstructures of the carbides for the three ingots, respectively. Obviously, the decrease of carbon content resulted in a decrease in the size of the carbides. Figure 8d, e, and f show the morphologies of precipitates in the interdendritic regions of the three ingots, respectively. The number and size of the precipitates for Ingot 2 are unchanged except for carbides, while the number and size of the precipitates in Ingot 3 decrease to some extent. In addition, the segregation coefficients of the Nb elements were measured and also calculated. The segregation coefficients of Nb in the three ingots were 0.42, 0.41, and 0.46, respectively. This indicates that the decrease of C content has little effect on the segregation of the Nb element, while the decrease of Nb content has a great effect on the segregation of GH4151. In conclusion, the reduction of C and Nb content is beneficial to improve the homogeneity of the microstructure of the as-cast GH4151, as shown in Fig. 8.

CONCLUSION

The solidification characteristics for GH4151 have been investigated in detail. The results obtained are as follows:

1. The phases in GH4151 were identified, consisting of a γ matrix, (Nb,Ti)C carbides, η phase, eutectic $(\gamma + \gamma')$, Laves phase, Ni_5Ce phase, and γ' phase.
2. The area of carbides and eutectic $(\gamma + \gamma')$ in the interdendritic region is large, and high Nb content existed in the η phase, which deteriorates the performance of the ingot and increases the tendency of hot tearing.
3. Nb provides significant segregation inclination and forms a large amount of carbides, eutectic
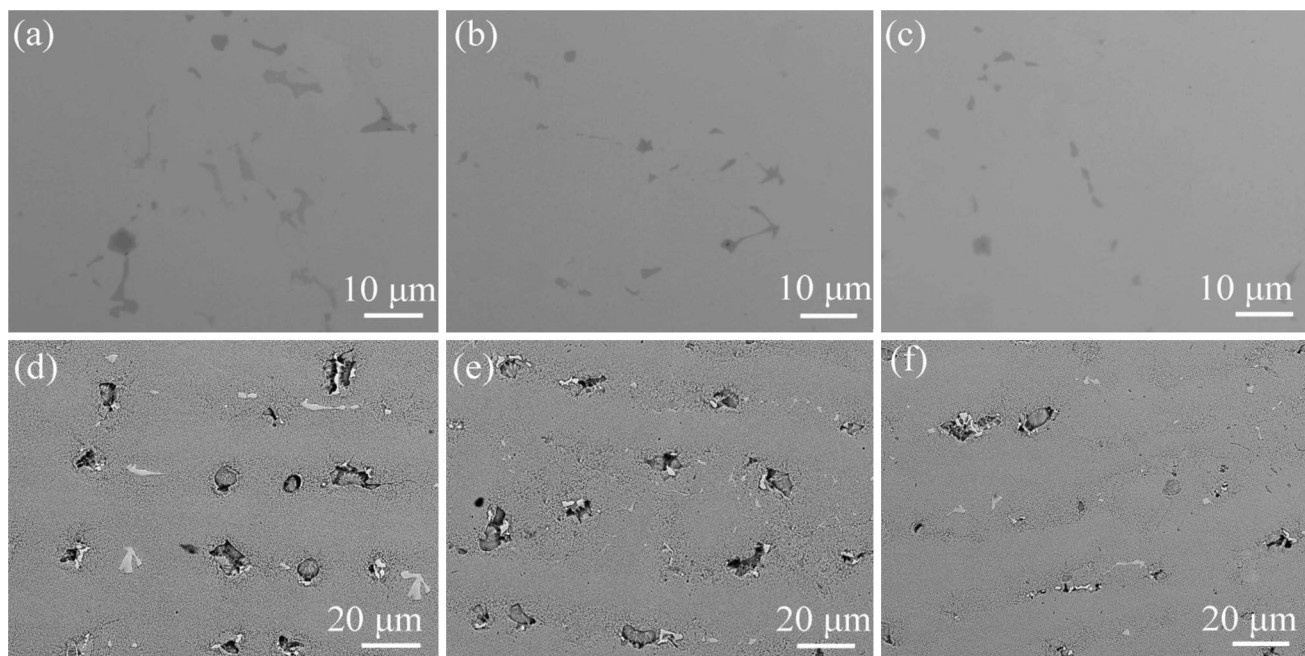

Fig. 8. The microstructure of three ingots: (a) carbide of ingot 1; (b) carbide of ingot 2; (c) carbide of ingot 3; (d) precipitates of ingot 1; (e) precipitates of ingot 2; (f) precipitates of ingot 3.

($\gamma + \gamma'$) phases, η phase, and Laves phases, which inevitably affect the number of the reinforced phases and then reduces the properties of the alloy.

4. The solidification sequence of GH4151 is determined as follows: L $\rightarrow$ L+γ $\rightarrow$ L+MC $\rightarrow$ L+η $\rightarrow$ L+($\gamma + \gamma'$) $\rightarrow$ L+Laves $\rightarrow$ L+Ni$_5$Ce, and γ $\rightarrow$ γ'.

5. It can be concluded from the EPMA quantitative analysis that Nb, Ti, Mo, V, and C are significantly enriched in the interdendritic region, whose degree of positive segregation is Nb > Ti > Mo > V, while Al, Co, Cr, W, and Ni are enriched in the dendritic arms, whose degree of negative segregation is W > Al > Ni > Co > Cr.

6. The reduction of C and Nb content is beneficial to improve the homogeneity of the microstructures of the as-cast GH4151.

ACKNOWLEDGEMENTS

REFERENCES

1. C.L. Jia, F.L. Zhang, K. Wei, and S.M. Lv, *J. Alloys Compd.* 770, 166 (2019).
2. Y.G. Tan, F. Liu, A.W. Zhang, D.W. Han, X.Y. Yao, W.W. Zhang, and W.-R. Sun, *Acta Metall. Sin-Engl.* (2019). https://doi.org/10.1007/s40195-019-00894-3.
3. Z.X. Shi, J.X. Dong, M.C. Zhang, and L. Zheng, *J. Alloys Compd.* 571, 168 (2013).
4. W.R. Sun, S.R. Guo, D.Z. Lu, and Z.O. Hu, *Mater. Lett.* 31, 195 (1997).
5. A.C. Wang, Y.Y. Li, C.G. Fan, and K. Yang, *Scr. Metall. Mater.* 31, 1695 (1994).
6. B.C. Yan, J. Zhang, and L.H. Lou, *Mater. Sci. Eng. A* 474, 39 (2008).
7. L. Qin, J. Shen, Q.D. Li, and Z. Shang, *J. Cryst. Growth* 466, 45 (2017).
8. S. Gao, Y.Z. Zhou, C.F. Li, and J.P. Cui, et al., *J. Alloys Compd.* 610, 589 (2014).
9. Z.K. Zhang and Z.F. Yue, *J. Alloys Compd.* 746, 84 (2018).
10. L. Zheng, C.Q. Gu, and Y.R. Zheng, *Scr. Mater.* 50, 435 (2004).
11. R. Liu, S. Xi, S. Kapoor, and X. Wu, *J. Mater. Sci.* 45, 6225 (2010).
12. M. Cieslak, T. Headley, A. Romig, and T. Kollie, *Metall. Mater. Trans. A* 19, 2319 (1988).
13. J. DuPont, M. Notis, A. Marder, and C. Robino, *Metall. Mater. Trans. A* 9, 2785 (1998).
14. L. Yu, Y. Zhao, S. Yang, and W. Sun, *J. Mater. Sci.* 45, 3448 (2010).
15. Z.J. Miao, A.D. Shan, J. Lu, and H.W. Song, *Mater. Sci. Technol.* 28, 334 (2012).
16. N. D'Souzaa and H.B. Dong, *Scr. Mater.* 56, 41 (2007).
17. N. D'Souza, H.B. Dong, M.G. Ardakani, and B.A. Shollock, *Scr. Mater.* 53, 729 (2005).
18. J. Zhang and R. Singer, *Acta Mater.* 50, 1869 (2002).
19. Y. Zhou, A. Volek, and R.F. Singer, *Metall. Mater. Trans. A* 36, 651 (2005).
20. G. Cao and S. Kou, *Mater. Sci. Eng. A* 417, 230 (2006).
21. N. D'Souza, M. Lekstrom, H.J. Dai, and B.A. Shollock, *Mater. Sci. Technol.* 23, 1085 (2007).
22. L. Zheng, C. Xiao, G. Zhang, and B. Han, *J. Alloys Compd.* 527, 176 (2012).
23. L. Zheng, G.Q. Zhang, C.B. Xiao, and T.L. Lee, *Scr. Mater.* 74, 84 (2014).
24. K.A. Al-Jarba and G.E. Fuchs, *JOM* 56, 50 (2004).
25. E.C. Caldwell, F.J. Fela, and G.E. Fuchs, *JOM* 56, 44 (2004).
26. C.L. Qiu, H.X. Chen, Q. Liu, and S. Yue, et al., *Mater. Charact.* 148, 330 (2019).
27. J. Madison, J.E. Spowart, D.J. Rowenhorst, and T.M. Pollock, *JOM* 60, 26 (2008).
28. J. Zhang and R. Singer, *Metall. Mater. Trans. A* 35, 1337 (2004).
29. F. Zupanic, T. Boncina, A. Krizman, and B. Markoli, et al., *Scr. Mater.* 46, 667 (2002).
30. S.M. Seo, J.H. Lee, and Y.S. Yoo, et al., *Metall. Mater. Trans. A* 42, 3150 (2011).
31. B. Liu, *JOM* 67, 3030 (2015).
32. L. Chapman, *J. Mater. Sci.* 39, 7229 (2004).
33. A. Shulga, *J. Alloys Compd.* 436, 155 (2007).
34. X. Zhao, L. Liu, Z. Yu, and W. Zhang, et al., *J. Mater. Sci.* 45, 6101 (2010).
35. K. Al-Jarba and G. Fuchs, *Mater. Sci. Eng. A* 373, 255 (2004).
36. D. Ma and U. Grafe, *Mater. Sci. Eng. A* 270, 339 (1999).
37. G. Fuchs and B. Boutwell, *Mater. Sci. Eng. A* 333, 72 (2002).
38. V. Wills and D. McCartney, *Mater. Sci. Eng. A* 145, 223 (1991).
39. A. Heckl, R. Rettig, S. Cenanovic, M. Göken, and R. Singer, *J. Cryst. Growth* 312, 2137 (2010).